primarily the result of a higher threshold for film optical damage at low temperature. Higher film stability at low temperatures likely explains the fact that, although we observed gain at both room and cryogenic temperatures, the clear signatures of stimulated emission were only detected at temperature $T = 80$ K. Figure 4 shows examples of stimulated emission spectra for close-packed films of TOPO-capped QDs with $R = 2.1$ nm (Fig. 4A) and ZnS-capped QDs with $R = 1.35$ nm (Fig. 4B), recorded at progressively higher pump levels. The films are optically pumped perpendicular to the sample plane, and the stimulated emission is detected at the edge of the films that act as optical waveguides. The development of a sharp stimulated emission peak is observed in both examples at wavelengths characteristic for the dot size, highlighting the size-controlled spectral tunability of the stimulated emission with dot size. The pump intensity dependence of this peak (Fig. 4, insets) shows a threshold behavior that is a clear signature of optical amplification. TOPO-capped QDs have poorer surface passivation and hence substantially smaller PL quantum yield than ZnS-capped dots. Nevertheless, because the Auger time scale is substantially faster than surface trapping in these dots, both types of samples showed similar gain properties.

Not all of the films that showed an optical gain in TA measurements demonstrated stimulated emission in PL spectra. This was probably due to differences in the optical quality of the films in their lateral directions. Images of QD samples taken with an optical microscope show chaotic networks of cracks on a sub–20-μm length scale. The surface density of cracks varied from sample to sample, leading to substantial differences in optical scattering losses in the lateral directions (across the cracks) for the millimeter lengths required for achieving large optical amplifications. Such differences in optical losses are much less pronounced in TA measurements where the samples are probed in a vertical direction (along the cracks) with the path length limited to 0.3 to 2 μm.

We demonstrated room and low-temperature optical gain in strongly confined nanocrystal QDs assembled as close-packed films (QD solids). Narrowband stimulated emission that is spectrally tunable with dot size and has a clear threshold behavior was also demonstrated for films cooled to liquid nitrogen temperature. These results provide a proof of principle for lasing in strongly confined nanocrystal QDs and should motivate the development of nanocrystal QD-based lasers and amplifiers over a broad spectral range.

Note added in proof: Recently, we were able to demonstrate room temperature narrowband stimulated emission in CdSe QD films.

References and Notes

1. D. Mehus and D. Evans, *Laser Focus World* **31**, 117 (1995).
2. A. Strass, *Laser Focus World* **30**, 79 (1994).
3. Y. Arakawa and H. Sakaki, *Appl. Phys. Lett.* **40**, 939 (1982).
4. M. Asada, Y. Miyamoto, Y. Suematsu, *IEEE J. Quantum Electron.* **QE-22**, 1915 (1986).
5. Al. L. Efros and A. L. Efros, *Sov. Phys. Semicond.* **16**, 772 (1982).
6. L. Brus, *J. Chem. Phys.* **79**, 5566 (1983).
7. N. N. Lebedson *et al.*, *Semiconductors* **28**, 832 (1994).
8. N. Kistaedter *et al.*, *Electron. Lett.* **30**, 1416 (1994).
9. M. Grundman, *Physica E* **5**, 167 (2000).
10. C. B. Murray, D. J. Norris, M. G. Bawendi, *J. Am. Chem. Soc.* **115**, 8706 (1993).
11. C. B. Murray, C. R. Kagan, M. G. Bawendi, *Science* **270**, 1335 (1995).
12. M. Nirmal *et al.*, *Phys. Rev. Lett.* **75**, 3728 (1995).
13. D. J. Norris, Al. L. Efros, M. Rosen, M. G. Bawendi, *Phys. Rev. B* **53**, 16347 (1996).
14. V. I. Klimov, A. A. Mikhailovsky, D. W. McBranch, C. A. Leatherdale, M. G. Bawendi, *Science* **287**, 1011 (2000).
15. V. S. Dneprovskii, V. I. Klimov, D. K. Okorokov, Yu. V. Vandyshev, *Solid State Commun.* **81**, 227 (1992).
16. J. Butty, Y. Z. Hu, N. Peyghambarian, Y. H. Kao, J. D. Mackenzie, *Appl. Phys. Lett.* **67**, 2672 (1995).
17. Y. Z. Hu, H. Gieβen, N. Peyghambaeian, S. W. Koch, *Phys. Rev. B* **53**, 4814 (1996).
18. H. Gieβen *et al.*, *Phase Transitions* **68**, 59 (1999).
19. M. A. Hines and P. Guyot-Sionnest, *J. Phys. Chem.* **100**, 468 (1996).
20. B. O. Dabbousi *et al.*, *J. Phys. Chem.* **101**, 9463 (1997).
21. V. I. Klimov, *J. Phys. Chem. B* **104**, 6112 (2000).
22. ______ and D. McBranch, *Phys. Rev. Lett.* **80**, 4028 (1998).
23. Sub-ps temporal resolution in the PL up-conversion experiment was achieved by gating the sample emission in the nonlinear optical crystal with a sub-ps laser pulse. The sum-frequency signal generated in the crystal is proportional to an instant PL intensity at the moment defined by an arrival time of the gating pulse. By scanning the gating pulse with respect to the PL pulse and detecting the changes in the sum-frequency signal, one can obtain information about the PL temporal profile.
24. Unless specifically mentioned, the data shown in the paper were taken at room temperature.
25. V. I. Klimov, Ch. J. Schwarz, D. W. McBranch, C. A. Leatherdale, M. G. Bawendi, *Phys. Rev. B* **60**, R2177 (1999).
26. The QDs were initially size selected and thoroughly washed by sequential precipitations from butanol, using methanol as the nonsolvent. QD solids were then prepared by drop casting films from hexane/octane solutions; solvent evaporation yielded dry solid films. The solutions were filtered immediately before film deposition to limit aggregate formation and to enhance optical quality. To further minimize aggregate formation, the solutions could be further diluted, or additional TOPO could be added. Excess TOPO, however, could also result in a loss of optical quality because the TOPO can crystallize, yielding a clouded film with a visible fractal pattern.
27. Photogenerated carrier densities were estimated with $N_{eh} = J_p\sigma_a$ where J_p is the pump fluence (photons per cm^2) and σ_a is the QD absorption cross section estimated according to (*21*).
28. This work was supported by Los Alamos Directed Research and Development funds, under the auspices of the U.S. Department of Energy; by the Air Force Office of Scientific Research, under contract MIPR-99-0026; by the NSF–Materials Research Science and Engineering Center program under grant DMR-98-08941; and by the Harrison Spectroscopy Laboratory under grant NSF-CHE-97-08265. C.A.L., H.J.E., and M.G.B. are grateful to S. Carpenter and S. Miller for technical assistance.

28 June 2000; accepted 21 August 2000

Graphite Polyhedral Crystals

Yury Gogotsi,[1]*† Joseph A. Libera,[1] Nikolay Kalashnikov,[1]
Masahiro Yoshimura[2]

Polyhedral nano- and microstructures with shapes of faceted needles, rods, rings, barrels, and double-tipped pyramids, which we call graphite polyhedral crystals (GPCs), have been discovered. They were found in pores of glassy carbon. They have nanotube cores and graphite faces, and they can exhibit unusual sevenfold, ninefold, or more complex axial symmetry. Although some are giant radially extended nanotubes, Raman spectroscopy and transmission electron microscopy suggest GPCs have a degree of perfection higher than in multiwall nanotubes of similar size. The crystals are up to 1 micrometer in cross section and 5 micrometers in length, and they can probably be grown in much larger sizes. Preliminary results suggest a high electrical conductivity, strength, and chemical stability of GPC.

Both graphite whiskers (*1*) and carbon nanotubes (*2*) represent unusual forms of carbon based on the distortion of graphene sheets. Conventional graphite forms hexagonal plate-like crystals with a very weak bonding between graphene layers. Graphite whiskers, in which a graphene sheet rolls into a scroll (*1*), provide a benchmark against which the performance of carbon fibers is compared. The discovery of carbon nanotubes (*2*) demonstrated the possibility of making strong graphite crystals consisting of coaxial closed tubes and challenged the position of whiskers as the strongest material known (*3–9*).

We report another form of strong filament based on graphite but with a much different structure than those reported previously. They

---

[1] University of Illinois at Chicago, Department of Mechanical Engineering, Chicago, IL 60607, USA. [2] Tokyo Institute of Technology, Materials and Structures Laboratory, 4259 Nagatsuta, Midori-ku, Yokohama 226, Japan.

*To whom correspondence should be sent: gogotsi@drexel.edu

†Present address: Drexel University, Department of Materials Engineering, Philadelphia, PA 19104, USA.

were found in the micrometer-size pores of a common carbon material, glassy carbon (GC). Some particles in pores of GC have been reported previously, but the quality of published images (*10*) has not allowed an analysis of their shape or structure. Raman spectra suggested formation of graphitic carbon in pores of GC (*11*). We found and analyzed polyhedral carbon structures in pores of GL-200 GC, which is made by the Toyo Tanso Co. in Japan (*12*).

Fracture of GL-200 glassy carbon reveals pores that split along the fracture surface (Fig. 1A). All pores contain unique crystal shapes (Fig. 1), which consist of pure carbon and possess interbonded basal planes that are at fixed angles to each other. These objects can be described as graphite polyhedra. Their ordered graphitic structure was confirmed by transmission electron microscopy (TEM) studies (Fig. 2). The crystals reached diameters of 1 μm and lengths of 5 μm. We observed polyhedral carbon nanotubes with the cross section from 5 to 100 nm (Fig. 1, B and D), nanorods or whiskers having constant (Fig. 1C) or variable (Fig. 1, B and D) cross sections of 100 to 1000 nm, and faceted carbon rings (Fig. 1E). They may have different interplanar angles, and the number of facets observed varied from 7 to 14. Some possess a helical habit (Fig. 1, C and D), whereas others are axially true (Fig. 2A). Cross-sectional TEM analysis shows that GPCs have a regular crystal shape with equal faces (Fig. 2B) when measured with up to 1% accuracy. Sevenfold (Fig. 1C), ninefold (Figs. 1F and 2A), and more complex symmetries were observed.

Many rod- or barrel-shaped crystals end with a thin protruding needle (Figs. 1D and 2A) that appears to be a multiwall nanotube (Fig. 2C), typically with a core diameter of about 5 to 20 nm and a conical, dome-capped, or semitoroidal tip. Some needles showed contrast imbalance and asymmetric fringing in TEM that do not match the cylindrical tube model and demonstrate polyhedral geometry. It has been suggested that polygonization of nanotubes should occur as the size gets larger (*2*, *13*). However, the regular shape of GPCs shows that folding of the carbon cylinders was not stochastic, but followed certain crystallographic principles (fixed angles and/or number of facets). Semitoroidal capsules growing on nanotube cores have been reported (*4*), and the structure of GPC is similar. However, a surprisingly large number of ordered carbon layers (up to 1500) (Fig. 2D) grew on the core nanotube and resulted in complex axis-symmetric structures never reported previously. The crystal habits of the GPCs are based on the molecular symmetry of their nanotube cores, which are known to have a variable screw-axis structure (*5*).

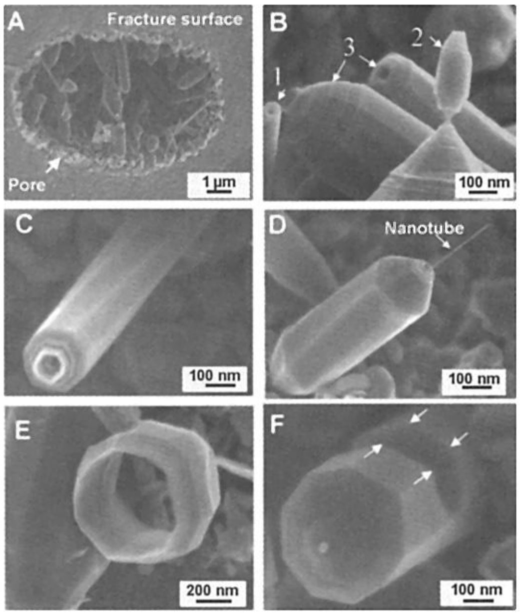

Fig. 1. SEMs of GPCs found in pores of glassy carbon. (**A**) Fracture surface, showing carbon nanotubes and GPCs growing in the pore. (**B**) Carbon nanotube (1), double cone (2), and microrods (3), which are typical structures. (**C**) Twisted rod with a heptagonal cross section. (**D**) Twisted GPC with a protruding nanotube. (**E**) Faceted ring that might be formed by pullout of the core structure similar to one in Fig. 2A. (**F**) Twisted rod that has a notch from crossing another GPC growing from the other side of the pore, which was removed when the pore fractured. Arrows mark edges of the interrupt.

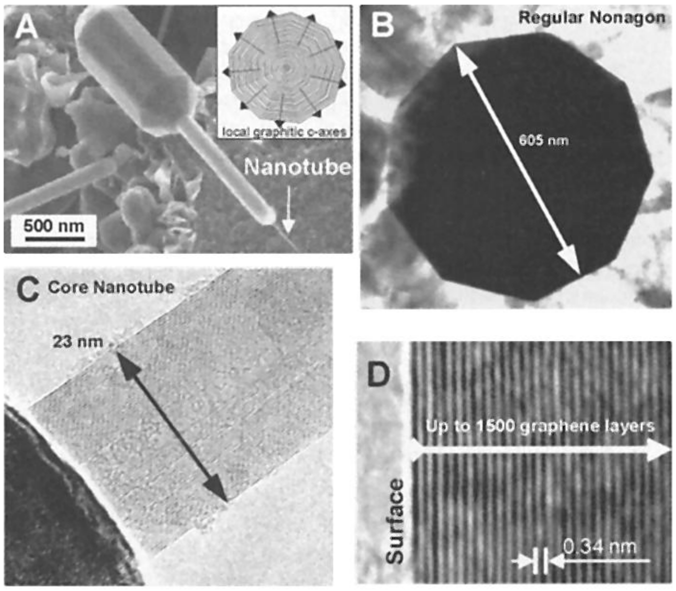

Fig. 2. Electron microscopy analysis of GPC structure. (**A**) SEM of a stylus-like crystal with a nanotube protruding from the tip. Inset shows a schematic of the GPC cross section. (**B**) View down the crystal axis showing that the imaged GPC is a regular nonagon in cross section. (**C**) A TEM image of a nanotube tip. (**D**) Typical lattice fringe image of the wall taken close to the surface along the axis of the GPC crystal showing a well-ordered graphitic structure with interplanar spacing of <0.34 nm.

The GC matrix is nongraphitic and produces broad D and G Raman bands of about the same intensity (*14*), whereas pores showed highly graphitic material with a weak D band and a narrow G band. A distinct aspect ratio of many of GPCs helped us to find them under microscope and record individual Raman spectra (Fig. 3). Submicrometer-sized GPCs are graphitic with the extincting D band and the G band of about the same width [full width at half maximum (FWHM) = 14 cm^{-1}] as in crystals of natural graphite (*14*). This can be explained by a smaller number of terminated graphene planes in GPC compared with a graphite crystal of the same size. The largest crystals were of sufficient size to enable selective micro-Raman analysis from the side face (Fig. 3, spectrum **a**) and from the tip (Fig. 3, spectrum **b**). Spectra from the crystal faces correspond to perfect graphite with a narrow G band and no D band, as expected from TEM analysis of GPC faces (Fig. 2D). Spectra from the tips (Fig. 3, spectrum **b**) feature an unusually strong second-order 2700 cm^{-1} band that exceeds in intensity the G band of graphite and a number of weak bands, including a clearly pronounced doublet at 184/192 cm^{-1}, which is in a fairly good agreement with spectra from single-wall nanotubes (*15*). Such spectra could result if all of the dangling bonds were eliminated by the formation of bent graphitic layers, as shown in Fig. 3 (TEM inset). The curvature of the outer layer (1.5 nm) is in good agreement with the average diameter of single-wall nanotubes, and the diameter of the inner loop (0.6 nm) is smaller than that of C_{60}-capped nanotubes. A similar process of elimination of dangling bonds was observed after heat treatment of oxidation-opened nanotubes at 2000°C (*16*) or filamentous graphite at 2800°C (*17*).

Well-defined curved termination of graphite sheets was also reported for carbon cones synthesized at 2200°C (*17*). On the basis of Raman spectra (narrow G band, no D band, and close to perfect graphite second-order spectrum) and TEM, GPCs have a higher perfection than multiwall nanotubes, which always show a distinct D band (*14*, *18*).

Unlike carbon fibers graphitized at 3000°C (*8*), GPCs do not have disordered carbon interlayers. Examination of the GPCs treated in supercritical water revealed no etching along the facet intersections, which suggests continuity of the graphene layers. However, some slow etching along graphene plane terminations was observed, as would be expected for the loop structures. Not coincidentally, there was no evidence of Raman bands at 184/192 cm^{-1} found in the treated samples. Moreover, unlike polygonized carbon black particles (*19*), GPCs do not have grain boundaries, which would have produced a strong D band in the Raman spectra.

An excellent confirmation of nonrandom growth and faceting of GPC is shown in Fig. 1F. Interrupted growth of a twisted GPC, caused by another crystal crossing with the original crystal in the initial stage of growth, continues after the cavity, resulting in the same number of facets as occurs in growth of crystallographically true crystals. Thus, the growth of GPCs follows axial symmetry. Only a few inorganic materials form low-dimensional tube-type crystals. Examples are cylindrical crystals of serpentine (*20*) and hollow whiskers of aluminum borates, which have square cross sections (*21*). However, we have observed GPC crystals with seven and more faces. We assume that the faceting of GPCs happened as a result of minimization of the surface energy compared with the cylindrical shape.

In the solid-state graphitization of amorphous carbon, crystallization starts in many places simultaneously to form randomly shaped faceted particles consisting of inter-grown polycrystals. GPCs are not polycrystals in this sense because they grow from the gas phase. Their folded and closed graphene planes differ from ordinary graphite but are similar to multiwall nanotubes, which can be thought of as tubular crystals of graphite. Thus, they could be considered giant polyhedral nanotubes with both a striking size and perfection (Fig. 1).

Microscopic observations provide some information on possible growth mechanisms of GPC. We assume that polyhedral nanotubes grow from C-H(N_2) gas trapped in pores during carbonization at 2000°C. Although trace amounts of iron were present in the material, energy dispersive spectroscopy (EDS) did not show any metal impurities in pores, lending support to a noncatalytic growth, similar to that of some carbon nanotubes (*22*), which can grow by addition of carbon hexagons, pentagons, and heptagons. Closure of the central (core) nanotube can occur due to pentagons giving rise to a curved geometry at the tip (*23*). Growth of GPC by both axial extension and radial thickening may result in pyramidal or rounded tip shapes (Fig. 1B). The high perfection of GPCs can be explained by their slow growth at temperatures of about 2000°C, which are higher than that for pyrolytic nanotubes (~1000°C).

They appear to have conductivity and optical properties similar to graphite. They have a high chemical stability and survive autoclave conditions (*12*) that lead to complete dissolution of GC. GPC did not shatter in pieces when GC was crushed to reveal pore structures, or when hydrothermally treated samples were ground for TEM or Raman studies. We did not find any obvious fracture surfaces (except a few nanotube tips); however, edges and corners of some of particles were damaged. The presence of rings (Fig. 1E) suggests the possibility of pullout of the inner core, as was observed for vapor-grown fibers (*24*). We expect a GPC to have at least the mechanical properties of graphite whiskers [a Young's modulus of ~800 GPa and strength of ~20 GPa (*1*)] along the axis, and probably that of nanotubes, approaching the theoretical limit for graphite. Nanoindentation tests of polished pores containing GPCs resulted in hardness values up to 5.8 GPa, compared with 3.2 GPa for glassy carbon and about 1 GPa for graphite. The Young's modulus of GPC regions was more than twice that of glassy carbon (49 and 23 GPa, respectively). The polyhedral structure of GPCs provides a higher rigidity compared with a cylindrical nanotube. Core nanotubes were straight and did not bend under their own weight or due to incorporated defects (Fig. 2A). Thus, GPCs could provide a better reinforcement to composites compared with cylindrical nanotubes, vapor-grown fibers, and whiskers because of their faceted shape. The carbon shells in GPC cannot rotate relative to each other, providing torsional stability to GPC. For twisted rods (Fig. 1C), "sword-in-sheath" failure will be prevented. However, even in axially symmetric crystals, toroidal edge termination may cross-link graphite layers and keep them together, increasing the strength of the whole particle.

GPCs represent a group of low-dimensional crystals with a variety of shapes, some of which were predicted [toroidal shape (*25*)] or experimentally observed in nanotubes (*26*), but have never been reported on the size scale or in the amounts that we found. It is probably not surprising that carbon, with its ability to exist in so many allotropic forms, produces a crystalline morphology not observed for other materials. The discovery of a previously unknown low-dimensional, axis-symmetric crystal may manifest the beginning of a new area of crystallography, similar to discovery of quasicrystals. The thickening of nanotubes by addition of carbon layers results in microscopic GPC particles up to 1 μm in thickness with a perfect graphitic structure and unusual sevenfold, ninefold, and more complex axial symmetry. Because their size is controlled by the pore size in GC (~5 μm), it should be possible to grow larger crystals. Thus, this finding may provide a way to grow nanotubes to the size of a pencil while still preserving their perfection. If this can be realized in practice, tailored micro- and macroscopic carbon shapes can be produced with a degree of perfection never seen before.

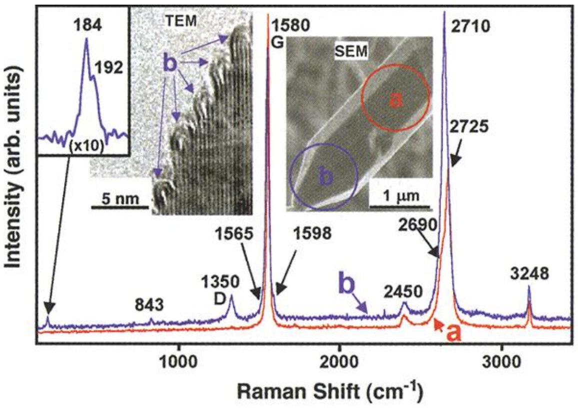

Fig. 3. First- and second-order Raman spectra obtained from (**a**) the faceted part and (**b**) the tip of a GPC shown in the SEM micrograph. The Raman spectra were taken by focusing the laser beam on an area of about 1 μm (circled on the SEM image); later, SEM and TEM images of the crystal were taken to better resolve its morphology. Absence of D band in the spectrum from the crystal face shows that the GPC is built of graphene sheets close to perfection. Raman bands at 184, 192, 843, 1350, and 1581 cm^{-1} (accompanied by shoulder bands at about 1565, 1600, and 1615 cm^{-1}) were observed in the spectra from the crystal tip. The TEM micrograph shows the semicylindrical termination of graphite planes in the tip region, which is believed to produce nanotube-like bands in Raman spectra. Bent graphitic layers (marked by arrows) look like two-layer nanotube tips in the cross section.

References and Notes

1. R. Bacon, *J. Appl. Phys.* **31**, 283 (1960).
2. S. Iijima, *Nature* **354**, 56 (1991).
3. Polyhedral carbon nanotubes have been reported (*4*–*7*) but did not receive much attention. Faceting of vapor-grown carbon fibers occurs after heating to 3000°C (*8*). Of all carbon fibers, those are the closest to crystalline graphite in crystal structure and properties. However, faceted carbon whiskers have not been reported. Partial graphitization and formation of polygons was observed after heat treatment of carbon black at

2800°C (*8*). Polyhedral nanoparticles (5 to 30 nm) made of concentric layers of closed graphene sheets with a nanoscale cavity in the center were produced at very high temperatures in arc plasma (*9*). They provide further evidence that nonplanar graphite crystals can exist. However, transformation of carbon polyhedra to onions under electron irradiation (*9*) suggested their instability. No other polyhedral carbon structures have been reported so far.

4. P. M. Ajayan, in *Carbon Nanotubes: Preparation and Properties*, T. W. Ebbesen, Ed. (CRC Press, Boca Raton, FL, 1997), pp. 111–138.
5. M. S. Dresselhaus, G. Dresselhaus, P. C. Eklund, *Science of Fullerenes and Carbon Nanotubes* (Academic Press, Burlington, MA, 1996).
6. S. Iijima, P. M. Ajayan, T. Ichihashi, *Phys. Rev. Lett.* **69**, 3100 (1992).
7. S. Iijima, *Mater. Res. Soc. Bull.* **19**, 43 (1994).
8. M. Endo, R. Saito, M. S. Dresselhaus, G. Dresselhaus, in *Carbon Nanotubes: Preparation and Properties*, T. W. Ebbesen, Ed. (CRC Press, Boca Raton, FL, 1997), pp. 35–110.
9. D. Ugarte, in *Carbon Nanotubes*, M. Endo, S. Iijima, M. S. Dresselhaus, Eds. (Pergamon, Oxford, 1996), pp. 163–167.
10. A. S. Fialkov, *Carbon, Intercalation Compounds and Composites on Its Base* (in Russian) (Aspect Press, Moscow, 1997).
11. K. Ray III and R. L. McCreery, *Anal. Chem.* **69**, 4680 (1997).
12. It was made from phenolic resin by carbonization at 2000°C in N_2 atmosphere at $\sim$10 torr. The density of GC was 1.48 g/cm^3 with an open porosity of $<$1%. Its microstructure and properties are typical of other GCs. Total content of impurities (Si, Al, Ca, Ti, V, and Fe) is $<$100 parts per million. Hydrothermal treatment under 100 MPa at 750°C for 24 hours dissolves the GC matrix and allows for separation of stable crystalline structures contained in the pores for TEM and Raman spectroscopy studies. The composition and structure of GPC were examined with the use of Raman spectroscopy, which is the most powerful technique for identifying carbon allotropes (*14*), and electron microscopy. A Renishaw 2000 Raman microspectrometer with an Ar ion laser (514.5-nm excitation wavelength) was used. The TEMs used were a JEOL 3010 (300 kV) with the lattice resolution of 0.14 nm and JEOL 2010F (200 kV) with the lattice resolution of 0.1 nm. High resolutions in the scanning mode were achieved with the use of the JSM-6320 field emission scanning electron microscope (SEM). This microscope is also fitted with a Noran Voyager EDS system with a light element x-ray detector analyzer. Particles were deposited onto a Si wafer or polished aluminum sample holder for Raman and SEM studies, or onto a lacy carbon grid for TEM analysis. Raman and SEM studies were also conducted on fracture surfaces of GC pieces.
13. M. Liu and J. M. Cowley, *Ultramicroscopy* **53**, 333 (1994).
14. M. S. Dresselhaus, G. Dresselhaus, M. A. Pimenta, P. C. Eklund, in *Analytical Applications of Raman Spectroscopy*, M. Pelletier, Ed. (Blackwell Science, Oxford, 1999), pp. 367–434.
15. A. M. Rao, *et al.*, *Science* **275**, 187 (1997).
16. D. Ugarte, T. Stockli, J.-M. Bonard, A. Chatelain, W. A. DeHeer, in *The Science and Technology of Carbon Nanotubes*, K. Tanaka, T. Yamabe, K. Fukui, Eds. (Elsevier, Amsterdam, 1999), pp. 128–142.
17. H. Murayama and T. Maeda, *Nature* **345**, 791 (1990).
18. H. Hiura, T. W. Ebbesen, K. Tanigaki, H. Takahashi, *Chem. Phys. Lett.* **202**, 509 (1993).
19. R. D. Heidenreich, W. M. Hess, L. L. Ban, *J. Appl. Crystallogr.* **1**, 1 (1968).
20. E. J. W. Wittaker, *Acta Cryst.* **21**, 461 (1966).
21. Y. G. Gogotsi, V. P. Yaroshenko, F. Porz, *J. Mater. Sci. Lett.* **11**, 308 (1992).
22. T. W. Ebbesen, *Phys. Today* **June**, 26 (1996).
23. C. J. Brabec, A. Maiti, C. Roland, J. Bernholc, *Chem. Phys. Lett.* **236**, 150 (1995).
24. K. Tanaka *et al.*, in *The Science and Technology of Carbon Nanotubes*, K. Tanaka, T. Yamabe, K. Fukui, Eds. (Elsevier, Amsterdam, 1999), pp. 143–152.
25. S. Ihara and S. Itoh, in *Carbon Nanotubes*, M. Endo, S. Iijima, M. S. Dresselhaus, Eds. (Pergamon, Oxford, 1996), pp. 77–85.
26. E. Osawa, M. Yoshida, M. Fujita, *Mater. Res. Soc. Bull.* **19**, 33 (1994).
27. Supported in part by the Campus Research Board of the University of Illinois at Chicago and the Research Institute for Solvothermal Technology, Japan. The electron microscopes used in this work are operated by the Research Resources Center at the University of Illinois at Chicago. The JEM-2010F purchase was supported by the NSF.

3 July 2000; accepted 6 September 2000

The Fall, Recovery, Orbit, and Composition of the Tagish Lake Meteorite: A New Type of Carbonaceous Chondrite

Peter G. Brown,[1] Alan R. Hildebrand,[3] Michael E. Zolensky,[4] Monica Grady,[5] Robert N. Clayton,[6] Toshiko K. Mayeda,[6] Edward Tagliaferri,[7] Richard Spalding,[8] Neil D. MacRae,[9] Eric L. Hoffman,[10] David W. Mittlefehldt,[11] John F. Wacker,[12] J. Andrew Bird,[3] Margaret D. Campbell,[1] Robert Carpenter,[9] Heather Gingerich,[9] Michael Glatiotis,[3] Erika Greiner,[9] Michael J. Mazur,[3] Phil JA. McCausland,[9] Howard Plotkin,[2] Tina Rubak Mazur[3]

The preatmospheric mass of the Tagish Lake meteoroid was about 200,000 kilograms. Its calculated orbit indicates affinity to the Apollo asteroids with a semimajor axis in the middle of the asteroid belt, consistent with a linkage to low-albedo C, D, and P type asteroids. The mineralogy, oxygen isotope, and bulk chemical composition of recovered samples of the Tagish Lake meteorite are intermediate between CM and CI meteorites. These data suggest that the Tagish Lake meteorite may be one of the most primitive solar system materials yet studied.

Carbonaceous chondrites represent the most chemically unfractionated class of meteorites known (*1*). Much of our present understanding of early solar nebular chemistry, particularly organic chemistry, comes from the characterization of chondrites. One group of carbonaceous chondrites, the CI1's, have particularly primitive, solar-like compositions (*2, 3*), although all studied samples have been almost completely aqueously altered on the parent asteroid. The carbonaceous chondrites have been associated with the C types of asteroids (*4, 5*) primarily on the basis of their similar reflectance spectra, but no direct dynamical evidence linking these meteorites to specific asteroid populations has been previously available. Here, we present the preatmospheric orbit, mass, and initial compositional characterization of the Tagish Lake meteorite.

The fireball producing the Tagish Lake meteorite occurred on 18 January 2000 at 16:43 UT. This exceptionally bright fireball was witnessed in dawn twilight throughout the Yukon and Northwest territories, northern British Columbia, and parts of Alaska. The fireball was detected by infrared (IR) and optical sensors aboard U.S. Department of Defense satellites. Optical measurements placed the energy of the light flash at 1.1×10^{12} J. Bolides of H-chondrite composition have been found to have light-energy conversions of $\sim$10% (*6*). A more realistic value for the present case is probably on the order of 5%, suggesting a total kinetic energy for the body of $\sim 2 \times 10^{13}$ J.

More than 70 eyewitnesses were interviewed to reconstruct the atmospheric trajec-

---

[1]Department of Physics and Astronomy, [2]Department of Philosophy, University of Western Ontario, London, Ontario N6A 3K7, Canada. [3]Department of Geology and Geophysics, University of Calgary, Calgary, Alberta T2N 1N4, Canada. [4]SN2, NASA Johnson Space Center, Houston, TX 77058, USA. [5]Department of Mineralogy, Natural History Museum, Cromwell Road, London SW7 5BD, UK. [6]Enrico Fermi Institute, Department of Chemistry, and Department of Geophysical Sciences, University of Chicago, 5640 South Ellis Avenue, Chicago, IL 60637, USA. [7]ET Space Systems, 5990 Worth Way, Camarillo, CA 93012, USA. [8]Sandia National Laboratories, Organization 5909, Mail Stop 0978, Post Office Box 5800, Albuquerque, NM 87185, USA. [9]Department of Earth Sciences, University of Western Ontario, London, Ontario N6A 5B7, Canada. [10]Activation Laboratories Ltd., 1336 Sandhill Drive, Ancaster, Ontario L9G 4V5, Canada. [11]Lockheed Martin SO, Houston, TX 77058, USA. [12]Pacific Northwest National Laboratory, Post Office Box 999, Richland, WA 99352, USA.